Frequency-Selectable Laser Source for Cosmic Microwave Background Experiments

Gabriel Rosen-Turits

Summer 2025

Abstract

Cosmic Microwave Background (CMB) experiments measure remnant radiation from the early universe and use that data to determine fundamental properties of the universe. We can constrain key parameters, such as r, the cosmic tensor-to-scalar ratio, and N_{eff}, the effective number of relativistic species, by analyzing the CMB power spectra. Improving our measurements of the CMB requires improving our instrument systematics, one of the most important of which is detector bandpass. Current experiments use a Fourier Transform Spectrometer (FTS) to measure bandpass. However, the FTS is systematics limited, and cannot achieve the accuracy needed to make improved CMB measurements. For this reason, we are developing a new instrument, the Frequency-Selectable Laser Source (FLS) to decrease the uncertainty in bandpass by an order of magnitude. In this paper, we describe work completed to support the version 2 upgrade to the FLS. Using ray-tracing software, we modeled the FLS optics to set physical tolerances for the new design. We also discuss the laser calibration, and future work to be completed in further development of the FLS upgrade.

1 Cosmic Microwave Background

1.1 Introduction

The Cosmic Microwave Background (CMB) is the remnant radiation from the early universe. It was discovered in 1964 by Arno Penzias and Robert W. Wilson [1]. The CMB formed when photons decoupled from baryons as the early universe cooled. This occurred at a time called last scattering, when the universe had cooled sufficiently such that hydrogen atoms could form. When these hydrogen atoms formed, photons became free to move through space. A sky map of the CMB, taken by the Planck Collaboration, can be seen in figure 1.

The CMB contains temperature anisotropies on the order of $\pm 300 \mu K$. The leading theory as to what caused these anisotropies is that they are the result of quantum density fluctuations at an early state of the universe. Then, a period of rapid expansion, known as inflation, led to these density fluctuations expanding to far larger scales [7].

Due to Thomson scattering in the early universe, the CMB is polarized. Polarization patterns take the form of E-modes and B-modes, named for the fact that they appear similar to electric

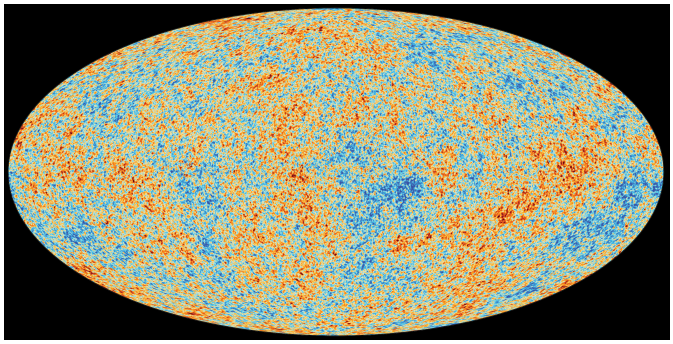

Figure 1: Foreground cleaned sky map of the CMB taken by Planck. This image is a high resolution rendering of the CMB, showing temperature anisotropies. (Figure from [5])

and magnetic fields respectively (see figure 2). The anisotropies that lead to E-modes come from density fluctuations, while the ones that would lead to B-modes are from gravitational waves [7]. So far, only E-modes and lensing B-modes (E-modes that are altered by gravitational lensing) have been detected [6]. The effort to detect inflationary B-modes is currently an experimental priority, as their discovery would be direct evidence of cosmological inflation.

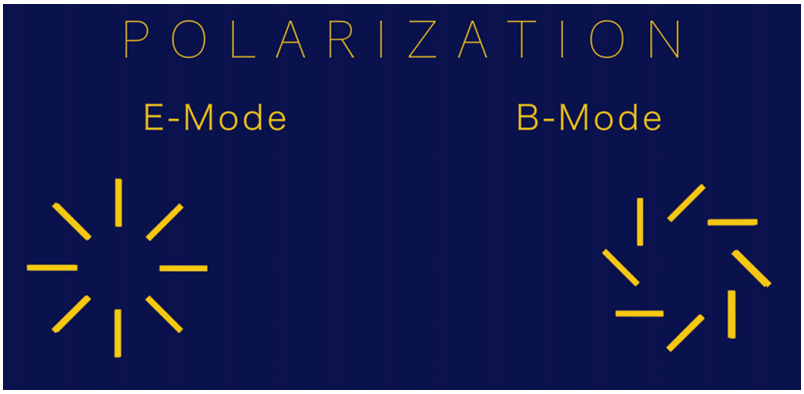

Figure 2: E-mode and B-mode visualization. This figure shows the difference in appearance between polarization modes. (Figure from [9])

When studying the properties of the CMB, we often transform our data from map space to power spectra. By doing so, we can analyze our signal vs. the multipole number ℓ (which can be thought of similarly to an angular frequency).

1.2 Science Goals

1.2.1 Tensor to Scalar Power Ratio, r

Constraining r, the ratio of the power of tensor modes to scalar modes in the CMB, is a key science goal. Currently, our best measurements bound $r \leq 0.032$ and $\sigma(r) = 0.014$ [8] [13]. Specific values of r correlate with different theories of inflation. To study r, we probe the low-ℓ end of the B-mode power spectrum.

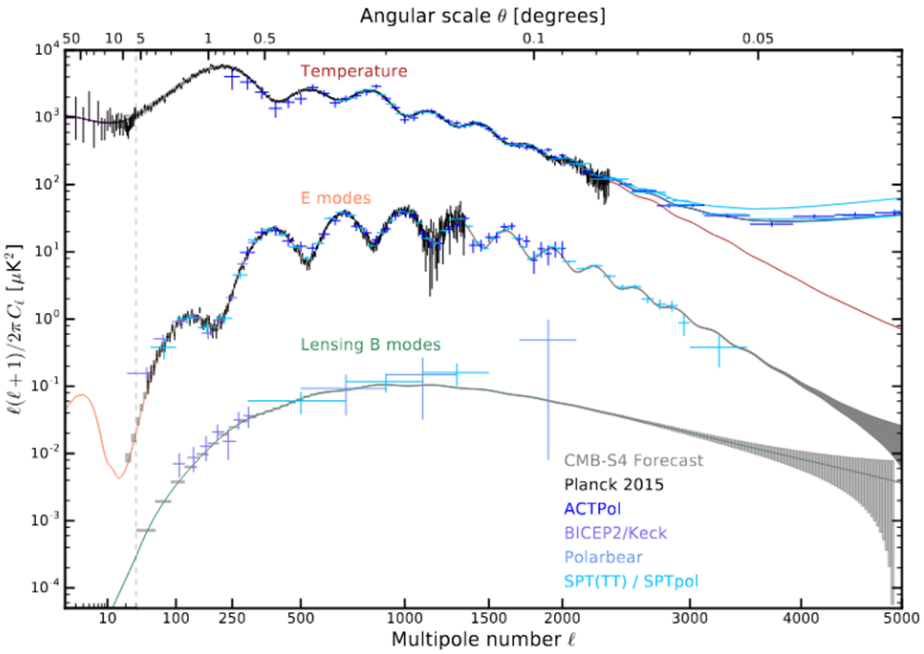

Figure 3: CMB Power Spectra. This figure shows the signal from temperature and polarization modes measured in the CMB. Contained in the shape of this curve is key information pertaining to cosmological parameters. (Figure from [2])

1.2.2 Effective Number of Relativistic Species N_{eff}

Another science goal being pursued through attempts to more accurately measure the power spectrum is N_{eff}, or the effective number of relativistic species. Measuring N_{eff} through the power spectrum is a model-independent way to study dark matter candidates. A higher value of N_{eff} is correlated with a more horizontally stretched power spectrum, as can be seen in figure 4. The currently accepted range of values for N_{eff} is ≥ 3.044 [10].

1.2.3 Sunyaev-Zeldovich Effect

A third science goal that cosmologists are attempting to measure is the Sunyaev-Zeldovich Effect. This effect is due to CMB photons being distorted through interactions with galaxy clusters. Studying this effect allows for better understanding of the evolution of large scale structure [4].

2 Technical Introduction

2.1 Bandpass

Modern CMB experiments use multichroic transition edge sensor (TES) bolometers to make detections [2]. Antennas allow us to sort polarization directions. Once the signal reaches a detector, the

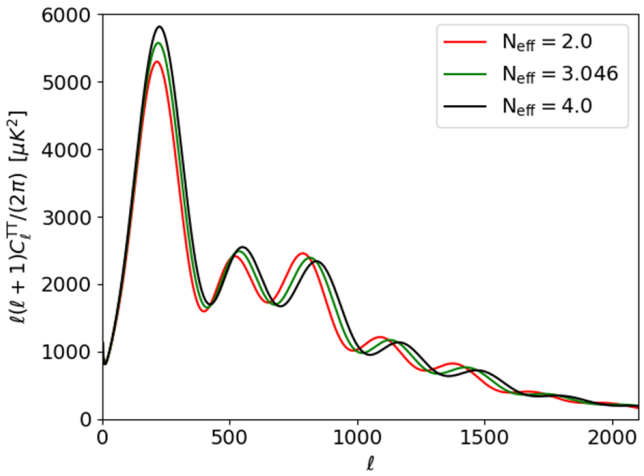

Figure 4: Simulated Power Spectra for Different N_{eff}. The variations in the spectra with N_{eff} allows us to constrain N_{eff} using CMB measurements. (Figure from [3])

detector will respond if it is tuned to the matching frequency. Bandpass refers to the range of frequencies a detector will respond to, as well as the detector gain in that range. A plot demonstrating bandpass can be seen in figure 5.

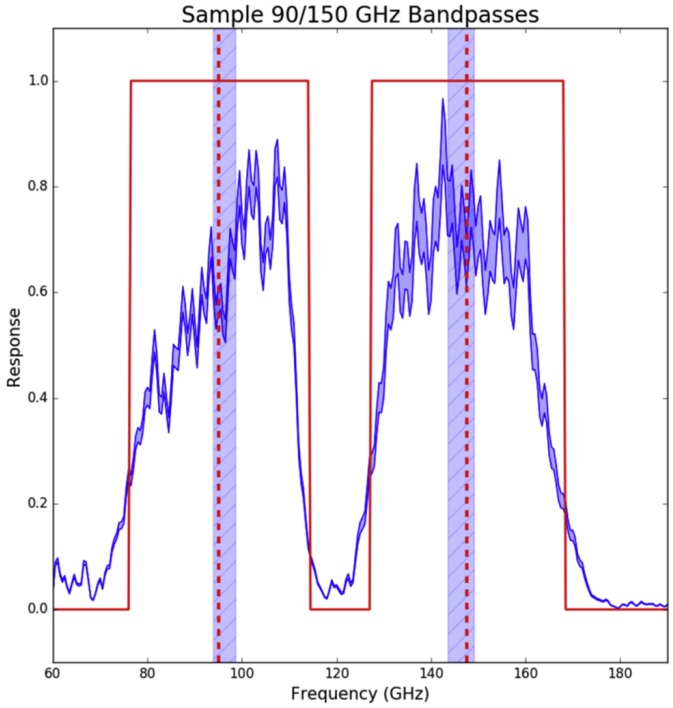

Figure 5: Simulated Bandpasses. In red, an ideal "top hat" bandpass is shown, with uniform response in the detector band and zero out-of-band response. The blue shows a more realistic bandpass. The complexity of real bandpasses necessitates that bandpass be characterized. (Figure from [14])

The ideal bandpass is modeled as a "top hat," detecting uniform signal within its range and none outside of it. However, we expect detector responses to be more complex, so we have to characterize them in order to improve the uncertainty of the experiments. Uncertainties in bandpass propagate forward to uncertainty in scientific output such as r. (See figure 6)

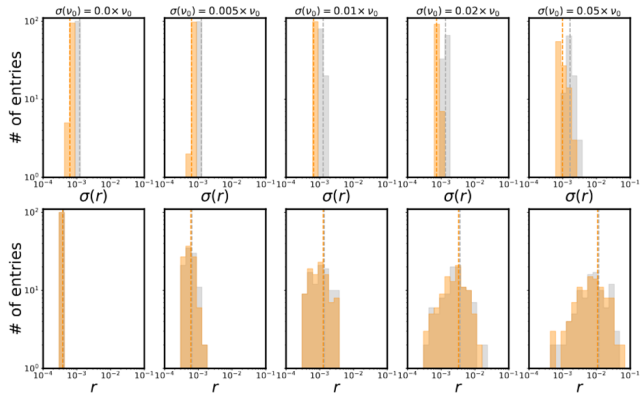

Figure 6: Uncertainty in r with Increasing Uncertainty in Frequency. The top five panels show the increase in $\sigma(r)$ with an increase in frequency uncertainty. The bottom five panels show the change in the distribution of r measurements for the same frequency uncertainties. This emphasizes the importance of minimizing frequency uncertainty, as frequency uncertainty propagates to uncertainty in r. (Figure from [14])

2.2 Measuring Bandpass

Currently, CMB experiments utilize a Fourier Transform Spectrometer (FTS) to measure bandpass. It measures the interference patterns between two beams of light, using a Michelson Interferometer. It is an effective tool, but it has systematics that place a lower bound on the remaining uncertainty in bandpass after its use. These systematics are not possible to improve within the design of the device.

For this reason, we are developing a Frequency-Selectable Laser Source (FLS) to be used in tandem with the FTS in order to more precisely measure bandpass. The FLS is an apparatus that contains a laser emitter, two parabolic mirrors, and a series of attenuating prisms [11]. The laser is emitted from the source, which is a Toptica-made emitter with a range of 20-1200 GHz and a minimum step size of 0.01 GHz [12]. It then reflects off of the parabolic mirror, which collimates the laser. After hitting the parabolic mirror, it is reflected through a series of five attenuators, each of which decreases the intensity of the light by 95%, without changing its frequency. Then, after the series of attenuators, the beam reflects off of another parabolic mirror, which directs it toward a receiver. By using the FLS along with the FTS, we can decrease our current uncertainties in bandpass by an order of magnitude.

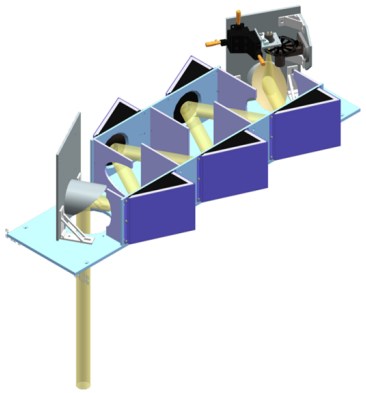

Figure 7: 3D Model of the FLS (Figure by H. Gutti, L. Saunders, and S. Simon)

3 FLS Version 2 Upgrade

3.1 Tolerancing

The FLS has already been demonstrated for studying bandpasses with real detectors. Experience with the prototype, though, has led to the need for an upgrade, which includes improved mechanical structure and testing methodology. Here, I discuss the work completed toward this upgrade. One part of this work is tolerancing the system, specifically for laser angle positioning. If the laser signal is too offset, it will fail to reflect off of all of the attenuators.

First, we have to find at what angle the light will reflect off of the parabolic mirror, as a function of its initial offset angle. In order to do this, we model the path of the light as two separate linear functions, one before it hits the mirror, and one after it reflects off of it. We calculate the initial linear function as:

$$y = (\cot \phi) * x + h \tag{1}$$

Here x and y are coordinates with $y = 0$ set at the bottom of the reflective surface of the parabolic mirror and $x = 0$ set the center of the emitter, ϕ is the offset angle, and h is the height of the emitter. Then, we define a function to describe the mirror. Given a mirror of height L, length l, and focal length p, we define the mirror as:

$$y = ax^2 + bx + c, \tag{2}$$

Where

$$a = \frac{1}{4p}, b = -\frac{L}{l}, c = \frac{L^2 p}{l^2} - \frac{(l^2 - 4Lp)^2}{16pl^2} \tag{3}$$

Then we calculate the intersection coordinates (X, Y) of the beam and mirror as:

$$X = \frac{-b + \cot\phi \pm \sqrt{(b - \cot\phi)^2 - 4a(c - h)}}{2a} \tag{4}$$

$$Y = (\cot\phi) * X + h \tag{5}$$

Following this, we calculate the normal to the surface of the mirror at the point of intersection as:

$$y = \left(-\frac{x - X}{(2aX) + b}\right) + Y \tag{6}$$

Once we have the norm, we can finally find the resultant line's equation, as

$$y = wx + f \tag{7}$$

Where

$$A = \cot\phi, B = h, C = -\frac{1}{2aX + b}, D = \frac{X}{2aX + b} + Y \tag{8}$$

$$w = \frac{2C + A(C^2 - 1)}{2AC + 1 - C^2} \tag{9}$$

$$f = \frac{2D(AC + 1) - B(C^2 + 1)}{2AC + 1 - C^2} \tag{10}$$

A visualization of this can be seen in figure 8.
From there, we calculate the resultant angle θ above the horizontal as:

$$\theta = \arctan(w) \tag{11}$$

Constant values for the FLS 2.0 can be found in table 1

Constant	Value (m)
L	0.10922
l	0.10922
p	0.0762
h	0.1972

Table 1: Bounds required for different conditions of the FLS apparatus

Then, with the FLS optics model built by L. Saunders using `pyoptools`[1], we find the maximum θ that the system can tolerate. The edge cases for this are shown in figure 9.

We then repeat that process, adding the tilt tolerance of the attenuators, and are able to obtain the bounds shown in Table 2 and the plot shown in figure 10.

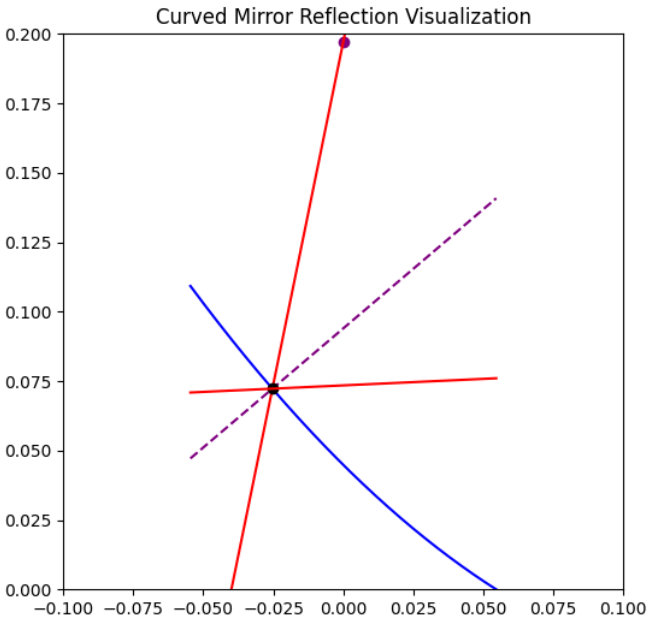

Figure 8: Parabolic Mirror Reflection Visualization. The laser ray (shown in red) reflects off of the parabolic mirror (blue), with normal line for reference (purple). Portions of the laser that appear below the mirror are a plotting artifact and do not represent real transmission.

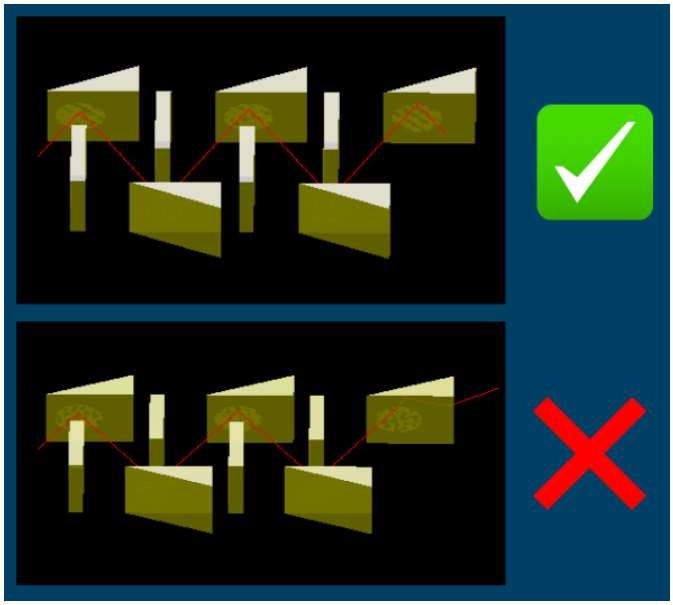

Figure 9: Visualization of Attenuator Edge Cases. The top image shows the maximum tolerable height for a single ray, where it reaches the final attenuator. The bottom shows the minimum height that is outside of the tolerance.

Next, we account for the full divergence of the laser, treating it as a cone as it leaves the source,

[1] https://pyoptools.readthedocs.io/

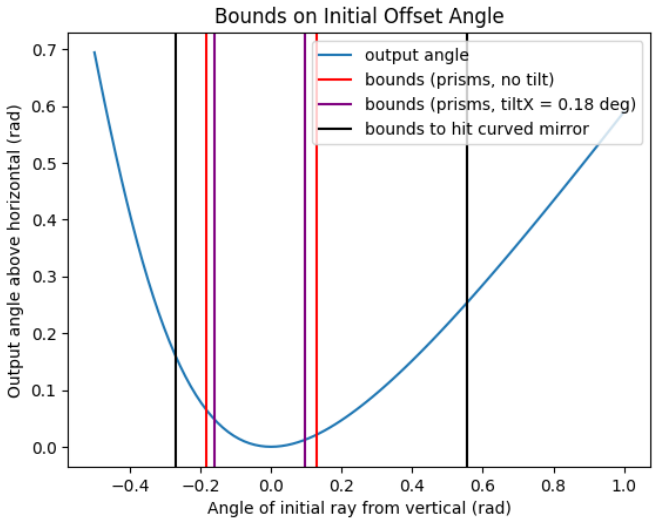

Figure 10: Angle After Parabolic Mirror Reflection vs Initial Offset Angle. All angles in radians. The maximum tolerable offset angles from the source in different scenarios are shown.

Bound Type	Lower Bound (rad)	Upper Bound (rad)
Mirror	-0.2701	0.5554
Attenuators (no tilt)	-0.1850	0.1300
Attenuators (tilt = 0.0031 rad)	-0.1600	0.0946

Table 2: Bounds required for the FLS apparatus. First, the bounds for the beam to reflect off of the initial parabolic mirror. Second, the bounds for it to reach all attenuators when they are not tilted. Third, the bounds for it to reach all attenuators with the tilt tolerance.

rather than as just an individual ray. It also means that rather than being interested in whether a beam will hit all of the attenuators or not for a given initial offset angle, we are interested in what percentage of the signal is lost for a beam that is centered at that offset angle. Each edge of the beam is initially displaced 6° from the center of the beam. A visual representation of this is shown in figure 11.

In order to measure the percentage of the signal lost, we treat the cone of light as a combination of many linear beams. We calculate the position of each of these beams at the point that it reaches the final attenuator. We then find the percentage of these linear beams that miss the final attenuator. By calculating this, and then recalculating with the tilt tolerance, we are able to obtain the plot seen in figure 12.

3.2 Laser Frequency Calibration

Another key part of the update to the FLS is ensuring that the frequency is stabilized when we are taking a measurement. The source of the original FLS had an issue where its frequency changed over time (see figure 13). It appears to be showing an exponential decay, with a time constant of 1.68 hours. We suspect that this decay is due to changes in the internal temperature of the laser

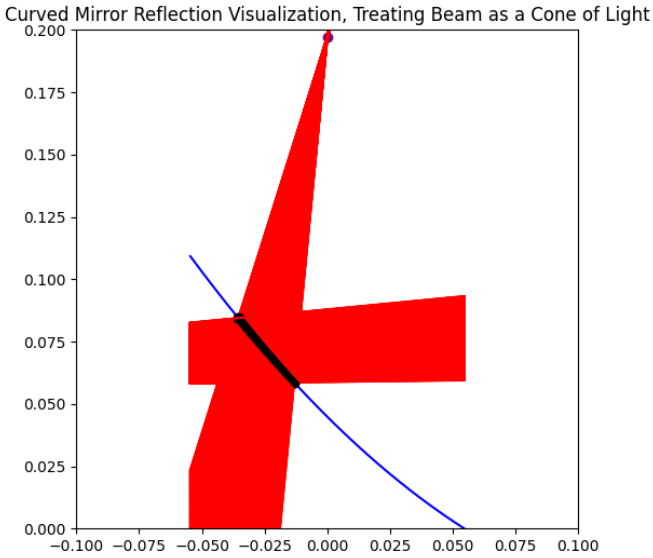

Figure 11: Visualization of the Laser Beam as a Cone of Light. Here we account for the laser's divergence. The full laser beam (red) reflects off of the curved mirror (blue). As in figure 8, the beam below the mirror is a plotting artifact and has no physical significance.

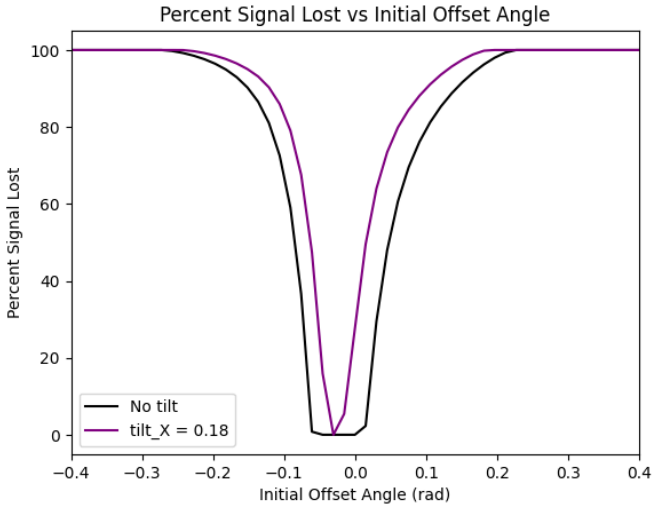

Figure 12: Percentage of Signal Lost as a Function of Initial Offset Angle. The loss is plotted both with and without a tilt in the prisms. Due to the geometry of the system, the curve is not centered at 0 rad.

source. Based on this behavior in the original Toptica Source, we now are aware that we will have to study the frequency behavior of the source for the FLS 2.0 as well.

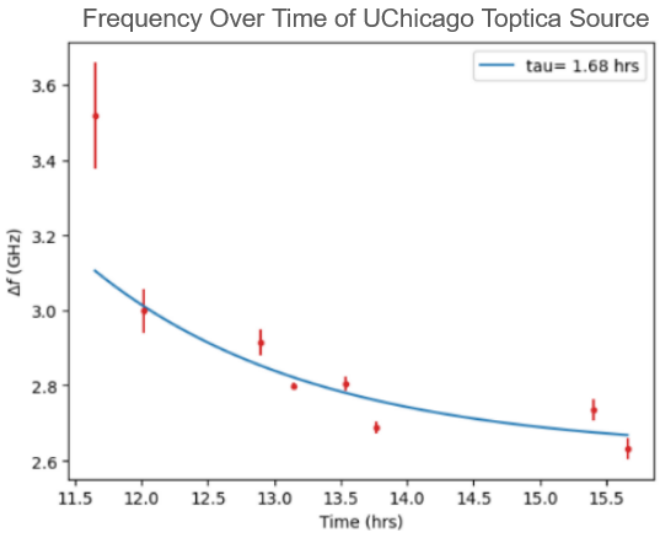

Figure 13: Frequency vs Time Dependence of the UChicago Toptica Source. The source exhibits a decay in frequency that could cause an issue for FLS use if not characterized.

3.3 Future Work

Once the FLS 2.0 is fully constructed, it will be fully characterized and then used for calibration on both existing and upcoming telescopes. Using the FLS will allow for a decrease in bandpass uncertainty by an order of magnitude. There are multiple steps still needed to get to that point. First, we have to assemble the FLS 2.0, based on the models that we have. Then, we have to calibrate the laser source to determine if it also exhibits frequency change over time or any overall frequency offset. If so, we must find its time constant and effective settling time. Following that, we will demonstrate its functionality and use it on detectors in the lab. Finally, the FLS 2.0 will be brought into the field for use.

4 Acknowledgments

This manuscript has been authored by FermiForward Discovery Group, LLC under Contract No. 89243024CSC000002 with the U.S. Department of Energy, Office of Science, Office of High Energy Physics.

This work was supported in part by the U.S. Department of Energy, Office of Science, Office of Workforce Development for Teachers and Scientists (WDTS) under the Science Undergraduate Laboratory Internships Program (SULI)

References

[1] Penzias, A. A. ; Wilson, R. W. A Measurement of Excess Antenna Temperature at 4080 Mc/s. *Astrophysical Journal*, July 1965.

[2] Kevork N. Abazajian, Peter Adshead, Zeeshan Ahmed, Steven W. Allen, David Alonso, Kam S. Arnold, Carlo Baccigalupi, James G. Bartlett, Nicholas Battaglia, Bradford A. Benson, Colin A. Bischoff, Julian Borrill, Victor Buza, Erminia Calabrese, Robert Caldwell, John E. Carlstrom, Clarence L. Chang, Thomas M. Crawford, Francis-Yan Cyr-Racine, Francesco De Bernardis, Tijmen de Haan, Sperello di Serego Alighieri, Joanna Dunkley, Cora Dvorkin, Josquin Errard, Giulio Fabbian, Stephen Feeney, Simone Ferraro, Jeffrey P. Filippini, Raphael Flauger, George M. Fuller, Vera Gluscevic, Daniel Green, Daniel Grin, Evan Grohs, Jason W. Henning, J. Colin Hill, Renee Hlozek, Gilbert Holder, William Holzapfel, Wayne Hu, Kevin M. Huffenberger, Reijo Keskitalo, Lloyd Knox, Arthur Kosowsky, John Kovac, Ely D. Kovetz, Chao-Lin Kuo, Akito Kusaka, Maude Le Jeune, Adrian T. Lee, Marc Lilley, Marilena Loverde, Mathew S. Madhavacheril, Adam Mantz, David J. E. Marsh, Jeffrey McMahon, Pieter Daniel Meerburg, Joel Meyers, Amber D. Miller, Julian B. Munoz, Ho Nam Nguyen, Michael D. Niemack, Marco Peloso, Julien Peloton, Levon Pogosian, Clement Pryke, Marco Raveri, Christian L. Reichardt, Graca Rocha, Aditya Rotti, Emmanuel Schaan, Marcel M. Schmittfull, Douglas Scott, Neelima Sehgal, Sarah Shandera, Blake D. Sherwin, Tristan L. Smith, Lorenzo Sorbo, Glenn D. Starkman, Kyle T. Story, Alexander van Engelen, Joaquin D. Vieira, Scott Watson, Nathan Whitehorn, and W. L. Kimmy Wu. Cmb-s4 science book, first edition, 2016.

[3] M. Aich, Y.-Z. Ma, W.-M. Dai, and J.-Q. Xia. How much primordial tensor mode is allowed? *Physical Review D*, 101, 2020.

[4] M Birkinshaw. The Sunyaev–Zel'dovich effect. *Physics Reports*, 310(2–3):97–195, March 1999.

[5] European Space Agency. Planck's view of the cosmic microwave background, 2019. https://www.esa.int/ESA_Multimedia/Images/2018/07/Planck_s_view_of_the_cosmic_microwave_background.

[6] D. Hanson, S. Hoover, A. Crites, P. A. R. Ade, K. A. Aird, J. E. Austermann, J. A. Beall, A. N. Bender, B. A. Benson, L. E. Bleem, J. J. Bock, J. E. Carlstrom, C. L. Chang, H. C. Chiang, H-M. Cho, A. Conley, T. M. Crawford, T. de Haan, M. A. Dobbs, W. Everett, J. Gallicchio, J. Gao, E. M. George, N. W. Halverson, N. Harrington, J. W. Henning, G. C. Hilton, G. P. Holder, W. L. Holzapfel, J. D. Hrubes, N. Huang, J. Hubmayr, K. D. Irwin, R. Keisler, L. Knox, A. T. Lee, E. Leitch, D. Li, C. Liang, D. Luong-Van, G. Marsden, J. J. McMahon, J. Mehl, S. S. Meyer, L. Mocanu, T. E. Montroy, T. Natoli, J. P. Nibarger, V. Novosad, S. Padin, C. Pryke, C. L. Reichardt, J. E. Ruhl, B. R. Saliwanchik, J. T. Sayre, K. K. Schaffer, B. Schulz, G. Smecher, A. A. Stark, K. T. Story, C. Tucker, K. Vanderlinde, J. D. Vieira, M. P. Viero, G. Wang, V. Yefremenko, O. Zahn, and M. Zemcov. Detection of b-mode polarization in the cosmic microwave background with data from the south pole telescope. *Physical Review Letters*, 111(14), September 2013.

[7] W. Hu. Wayne Hu's tutorials, 2001. https://background.uchicago.edu/index.html.

[8] NASA. Lambda - graphics: Upper limits on the tensor to scalar power ratio, 2023. https://lambda.gsfc.nasa.gov/education/lambda_graphics/r_upper_limits.html.

[9] Goddard Space Flight Center NASA. Piper infographic, 2018. https://svs.gsfc.nasa.gov/12968.

[10] S. Navas et al. Review of particle physics. *Phys. Rev. D*, 110(3):030001, 2024.

[11] Shreya Sutariya, Kathleen Harrington, Carlos Sierra, Thomas Alford, Erin Healy, Lauren J. Saunders, Sara M. Simon, and Jeff McMahon. Bandpass calibration using a frequency-selectable laser source (fls). 2025 (in preparation).

[12] Toptica Photonics AG. *TeraScan 1550 TeraBeam 1550 Manual*, 2019.

[13] M. Tristram, A.J. Banday, K.M. Górski, R. Keskitalo, C.R. Lawrence, K.J. Andersen, R.B. Barreiro, J. Borrill, L.P.L. Colombo, H.K. Eriksen, R. Fernandez-Cobos, T.S. Kisner, E. Martínez-González, B. Partridge, D. Scott, T.L. Svalheim, and I.K. Wehus. Improved limits on the tensor-to-scalar ratio using bicep and planck. *Physical Review D*, 105(8), April 2022.

[14] J. T. Ward, D. Alonso, J. Errard, M. J. Devlin, and M. Hasselfield. The effects of bandpass variations on foreground removal forecasts for future cmb experiments. *The Astrophysical Journal*, 861, 2018.